PAPER

Check for updates

Fragmentation patterns of DNA-stabilized silver nanoclusters under mass spectrometry†

Rweetuparna Guha, [ID] [a] Sami Malola, [e] Malak Rafik, [a] Maya Khatun, [e] Anna Gonzàlez-Rosell, [ID] [a] Hannu Häkkinen [ID] [e] and Stacy M. Copp [ID] *[a,b,c,d]

DNA-stabilized silver nanoclusters (Ag_N-DNAs) are emitters with tuneable structures and photophysical properties. While understanding of the sequence–structure–property relationships of Ag_N-DNAs has advanced significantly, their chemical transformations and degradation pathways are far less understood. To advance understanding of these pathways, we analysed the fragmentation products of 21 different red and NIR Ag_N-DNAs using negative ion mode electrospray ionization mass spectrometry (ESI-MS). Ag_N-DNAs were found to lose Ag^+ under ESI-MS conditions, and sufficient loss of silver atoms can lead to a transition to a lesser number of effective valence electrons, N_0. Of more than 400 mass spectral peaks analysed, only even values of N_0 were identified, suggesting that solution-phase Ag_N-DNAs with odd values of N_0 are unlikely to be stable. Ag_N-DNAs stabilized by three DNA strands were found to fragment significantly more than Ag_N-DNAs stabilized by two DNA strands. Moreover, the fragmentation behaviour depends strongly on the DNA template sequence, with diverse fragmentation patterns even for Ag_N-DNAs with similar molecular formulae. Molecular dynamics simulations, with forces calculated from density functional theory, of the fragmentation of $(DNA)_2(Ag_{16}Cl_2)^{8+}$ with a known crystal structure show that the 6-electron $Ag_{16}Cl_2$ core fragments into a 4-electron Ag_{10} and a 2-electron Ag_6, preserving electron-pairing rules even at early stages of the fragmentation process, in agreement with experimental observation. These findings provide new insights into the mechanisms by which Ag_N-DNAs degrade and transform, with relevance for their applications in sensing and biomedical applications.

Introduction

DNA-stabilized silver nanoclusters (Ag_N-DNAs) are emerging as promising emitters for biological sensing and imaging applications due to their uniquely tunable photophysical properties and biocompatible surface chemistries. These ultrasmall nanoparticles (1–3 nm) range in size from about 10 to 30 Ag atoms and are encapsulated by 1–3 single-stranded DNA oligomers. The DNA oligomer acts as a multidentate ligand for silver, stabilizing Ag_N-DNAs with exceptionally high atomic precision.

The DNA sequence encodes the size and shape of the Ag_N-DNA, ultimately dictating its photophysical properties.[1] The properties of Ag_N-DNAs can also be sensitive to changes in the local environment,[2] which has been harnessed by strategies using probes such as NanoCluster Beacons to sense nucleic acids and other analytes.[3,4] Ag_N-DNAs exhibit many favourable properties as emitters: a wide palette of emission wavelengths ranging from visible to near-infrared (NIR),[1,5] as well as high Stokes shifts[6] and quantum yields,[7] especially as compared to those of commonly used NIR organic dyes. These properties have driven recent interest in NIR Ag_N-DNAs as candidates for bioimaging in the tissue transparency windows.

The fundamental understanding of Ag_N-DNA sequence–structure–property relationships has been significantly advanced by studies of atomically precise Ag_N-DNAs purified by high-performance liquid chromatography (HPLC) and sized by high-resolution electrospray ionization mass spectrometry (ESI-MS).[5] In contrast, chemical transformations involving Ag_N-DNAs remain poorly understood. The clearly demonstrated applications of Ag_N-DNAs in biosensing and imaging[3,8–11] demand an in-depth understanding of such mechanisms, which may underlie colorimetry-based sensing and are important for understanding the possible decompo-

[a]*Department of Materials Science and Engineering, University of California, Irvine, CA 92697, USA. E-mail: stacy.copp@uci.edu*
[b]*Department of Physics and Astronomy, University of California, Irvine, CA 92697, USA*
[c]*Department of Chemical and Biomolecular Engineering, University of California, Irvine, CA 92697, USA*
[d]*Department of Chemistry, University of California, Irvine, CA 92697, USA*
[e]*Departments of Chemistry and Physics, Nanoscience Center, University of Jyväskylä, Jyväskylä 40014, Finland*

†Electronic supplementary information (ESI) available: Materials and experimental methods; mass spectra and associated calculated mass distributions; details of simulation and modelling. See DOI: https://doi.org/10.1039/d4nr03533j

sition routes of Ag_N-DNAs *in vivo*. Recent work by Petty and coauthors investigated the degradation of one Ag_{10}-DNA under laser-driven photobleaching, providing some of the first insights into Ag_N-DNA decomposition.[12] This type of investigation is lacking for nearly all other Ag_N-DNAs reported to date.

Mass spectrometry offers a sensitive way to investigate metal nanocluster stability and reactions in the gas phase. For example, collision-induced dissociation (CID) and time-dependent trapped ion mobility spectrometry (TIMS) have been used to elucidate the effects of ligands, ligand–metal core interactions, and structures of intermediates formed during the dissociation of monolayer-protected noble metal clusters.[13–17] These experimental approaches have also improved understanding of inter-cluster reactions of reactive coinage metal clusters during solution-phase formation of alloy clusters.[18,19] Mass spectrometry could also provide insights into how Ag_N-DNA species transform or degrade. However, unlike monolayer-protected metal nanoclusters, which are typically stabilized by small molecules such as thiols,[20,21] phosphines,[22] and carbenes,[23] Ag_N-DNAs are stabilized by much bulkier DNA oligomer ligands, which makes it more challenging to use ESI-MS to determine nanocluster composition. Ag_N-DNA mass spectra can be acquired under native-like ESI-MS conditions, using techniques that were developed to preserve the solution-phase structure of noncovalent nucleic acid complexes.[1,24–27] During ESI-induced desolvation, liquid is forced through a needle on which a voltage is applied in order to create an aerosol. As the resulting droplets evaporate, the negatively charged phosphate backbones are partially protonated due to proton transfer from ammonium ions to phosphate groups.[28] Even under such conditions, mass spectra of Ag_N-DNAs also show the presence of multiple smaller-mass fragments with varying silver contents. These include nanoclusters with fewer valence electrons, which are known to have distinct fluorescence excitation and emission spectra.[24,27,29–32] Because of the optical purity[33] exhibited by the HPLC-purified Ag_N-DNAs that have been examined by ESI-MS, these smaller-mass products are attributed to fragmentation of Ag_N-DNAs during ESI-MS. We hypothesize that this fragmentation could be used to probe the chemical properties of Ag_N-DNAs without CID.

Based on this hypothesis, we investigated a large set of 21 different Ag_N-DNA species with diverse ligand compositions, nanocluster silver contents, N_{Ag}, and numbers of effective valence electrons, N_0. We found that the patterns of fragmentation products formed during ESI-MS depend strongly on the DNA template sequence and ligand chemistry of the Ag_N-DNA species. In all cases, Ag_N-DNAs are observed to lose Ag^+ in the gas phase while preserving N_0. When N_{Ag} reaches a lower limit, which is unique to each Ag_N-DNA species, the fragments can transition to smaller values of N_0. Even in these transient species, only even values of N_0 are observed. Density functional theory (DFT) provides insights into the dissociation mechanism of $(DNA)_2(Ag_{16}Cl_2)^{8+}$ with a known X-ray crystal structure,[34] whose $N_0 = 6$ Ag_{16} core dissociates into two smaller Ag_6

and Ag_{10} species with N_0 values of 2 and 4, respectively. This analysis provides key insights into the lability of Ag_N-DNAs, including mechanisms that may underlie behaviour of relevance to Ag_N-DNA-based sensing mechanisms and to their degradation in biological settings, of relevance to properties such as cytotoxicity.

Results

21 Ag_N-DNAs were selected from a library designed using machine learning-aided high-throughput experiments.[35–38] Ag_N-DNAs were purified using HPLC to obtain atomically precise Ag_N-DNAs with high purity, and optical spectra confirm the presence of a single emissive species in the HPLC-purified samples.[30] These Ag_N-DNAs exhibit peak emission at the far red to near-infrared (NIR) spectral border and varying molecular formulae (Table 1). As in previous work, the molecular formula is assigned to the nanocluster product with the greatest number of silver atoms (N_{Ag}) resolved in the mass spectrum, using negative ion mode ESI-MS.[30] (As noted previously, N_{Ag} may not represent the silver content of the nanocluster core because additional Ag^+ could bind to the DNA ligand shell without being incorporated into the nanocluster core. Accurate assignment of the silver content of the Ag_N core requires comparing Ag_N-DNA mass spectra with X-ray crystal structures, which are presently available for very few Ag_N-DNAs.[34,39,40]) Negative ion mode ESI-MS is used for Ag_N-DNA characterization because this is a sensitive method for studying noncovalent nucleic acid complexes. At neutral pH, phosphate groups are deprotonated and nucleobases are typically neutral. For more details regarding the utility of negative ion mode ESI-MS for nucleic acids, readers are directed to a comprehensive review by Largy *et al.*[28] Synthesis procedures, HPLC chromatograms, and mass spectra have been previously reported for all Ag_N-DNAs except for **I.8**, which is shown in Fig. S1 and S2.†[2,29,30] For clarity, the mass spectra of all other Ag_N-DNAs are shown in Fig. S3–S20.†

The mass spectrum is used to determine the Ag_N-DNA molecular formula using previously established methods,[26,41] which are detailed in ESI section 3.1.† The experimental isotopic distribution for a specific product is compared to calculated distributions to determine the total number of DNA strands (n_s), the total silver content (N), and the overall charge of the nanocluster (Q_c) of the Ag_N-DNA. (Note that if chlorido ligands are present, these will contribute to the calculation of Q_c.) The molecular formula is denoted as $(DNA)_{n_s}(Ag_N)^{Q_c+}$, and N_0 is calculated as $N_0 = N - Q_c$. For example, **I.1** has the molecular formula, $(DNA)_2(Ag_{20})^{14+}$ and has $N_0 = 20 - 14 = 6$ valence electrons (Table 1).

Mass spectra for all Ag_N-DNA species were acquired using identical ESI-MS conditions. Bethur *et al.* previously reported that parameters such as capillary voltage, desolvation temperature, desolvation gas flow, and injection flow rate influence the relative intensities of the mass spectral peaks of DNA-Ag^+ complexes.[42] Thus, uniform ESI-MS conditions must be used for

Table 1 DNA template sequences and compositions of Ag_N-DNAs, determined by ESI-MS[2,29,30]

Name	DNA sequence (5′ to 3′)	Chemical composition	Molecular formula
Group I: Ag_N-DNAs containing $n_s = 2$ and $N_0 = 6$			
I.1	GTCCGGGCCA	$C_{192}H_{244}N_{78}O_{116}P_{18}Ag_{20}$	$(DNA)_2(Ag_{20})^{14+}$
I.2	ACCAATGACC	$C_{192}H_{244}N_{78}O_{110}P_{18}Ag_{15}$	$(DNA)_2(Ag_{15})^{9+}$
I.3	CCAGCCCGGA	$C_{190}H_{242}N_{80}O_{112}P_{18}Ag_{18}$	$(DNA)_2(Ag_{18})^{12+}$
I.4	GTAGTCCCTA	$C_{194}H_{248}N_{70}O_{118}P_{18}Ag_{16}$	$(DNA)_2(Ag_{16})^{10+}$
I.5	ATCCCCTGTC	$C_{190}H_{248}N_{62}O_{120}P_{18}Ag_{17}$	$(DNA)_2(Ag_{17})^{11+}$
I.6	AGTCACGACA	$C_{194}H_{244}N_{82}O_{110}P_{18}Ag_{16}$	$(DNA)_2(Ag_{16})^{10+}$
I.7	GCCCCCCCGC	$C_{184}H_{242}N_{68}O_{116}P_{18}Ag_{14}$	$(DNA)_2(Ag_{14})^{8+}$
I.8	CCGGAATCCG	$C_{192}H_{244}N_{78}O_{114}P_{18}Ag_{20}$	$(DNA)_2(Ag_{20})^{14+}$
Group II: Ag_N-DNAs containing $n_s = 3$ and $N_0 = 6$			
II.1	CCCGGCCGAA	$C_{285}H_{363}N_{120}O_{168}P_{27}Ag_{18}$	$(DNA)_3(Ag_{18})^{12+}$
II.2	CCCGGAGAAG	$C_{291}H_{363}N_{132}O_{165}P_{27}Ag_{22}$	$(DNA)_3(Ag_{22})^{16+}$
II.3	CCTGGGGAAA	$C_{294}H_{366}N_{129}O_{168}P_{27}Ag_{16}$	$(DNA)_3(Ag_{16})^{10+}$
Group III: Ag_N-DNAs containing $n_s = 2$, chlorido ligands, and $N_0 = 6$			
III.1	AACCCCACGT	$C_{190}H_{244}N_{74}O_{112}P_{18}ClAg_{15}$	$(DNA)_2(Ag_{15}Cl)^{7+}$
III.2	CACCTAGCGA	$C_{192}H_{244}N_{78}O_{112}P_{18}Cl_2Ag_{16}$	$(DNA)_2(Ag_{16}Cl_2)^{8+}$
III.3	CACCAAGCGA	$C_{192}H_{242}N_{84}O_{108}P_{18}Cl_2Ag_{16}$	$(DNA)_2(Ag_{16}Cl_2)^{8+}$
III.4	CACCCAGCGA	$C_{190}H_{242}N_{80}O_{110}P_{18}Cl_2Ag_{16}$	$(DNA)_2(Ag_{16}Cl_2)^{8+}$
III.5	CACCGAGCGA	$C_{192}H_{242}N_{84}O_{110}P_{18}Cl_2Ag_{16}$	$(DNA)_2(Ag_{16}Cl_2)^{8+}$
III.6	CACCTAGCG_	$C_{172}H_{220}N_{68}O_{102}P_{16}Cl_2Ag_{16}$	$(DNA)_2(Ag_{16}Cl_2)^{8+}$
Group IV: Ag_N-DNAs containing $n_s = 2$ and $N_0 = 8$			
IV.1	GCGCAAGATG	$C_{196}H_{244}N_{86}O_{112}P_{18}Ag_{19}$	$(DNA)_2(Ag_{19})^{11+}$
IV.2	GACGACGGAT	$C_{196}H_{244}N_{86}O_{112}P_{18}Ag_{17}$	$(DNA)_2(Ag_{17})^{9+}$
IV.3	ATCTCCACAG	$C_{129}H_{246}N_{72}O_{114}P_{18}Ag_{16}$	$(DNA)_2(Ag_{16})^{8+}$
IV.4	AGGCGATCAT	$C_{196}H_{246}N_{80}O_{114}P_{18}Ag_{20}$	$(DNA)_2(Ag_{20})^{12+}$

all 21 Ag_N-DNAs studied here to allow direct comparison of fragmentation products resolved in their mass spectra. The selected ESI-MS conditions (Methods) were found to minimize the fragmentation of Ag_N-DNAs into smaller-mass products. We note that desolvation temperature affects the relative intensity of mass peaks at different charge states z (Fig. S22†) but does not affect the number of effective valence electrons of the Ag_N core, N_0, for each identified mass product (Fig. S23 and Table S1†). This supports that the experimental methods used here have relevance to more general chemical transformations of Ag_N-DNAs. Moreover, we did not observe any evidence of DNA oligomer fragmentation in any of the analyzed mass spectra, supporting that only the nanocluster fragments, and not the DNA oligomer itself. This is in contrast to past work that used activated electron photodetachment to fragment the DNA backbone and thereby gain structural insights into Ag_N-DNAs.[43]

Table 1 groups Ag_N-DNAs by their ligand composition, *i.e.* the number of ssDNA oligomers (n_s) and the presence or absence of chlorido ligands, and by N_0.[30] **Group I** Ag_N-DNAs have $N_0 = 6$ and $n_s = 2$. **Group II** Ag_N-DNAs contain $N_0 = 6$ and $n_s = 3$; these emitters exhibit the shortest Stokes shift among all four groups.[30] **Group III** Ag_N-DNAs exhibit $N_0 = 6$, $n_s = 2$, and additional chlorido ligands. These Ag_N-DNAs exhibit higher Stokes shifts than Ag_N-DNAs without chloridos[6] and are stable under physiologically relevant buffers. **Group IV** Ag_N-DNAs exhibit $N_0 = 8$ and $n_s = 2$, and two of these display microsecond-lived luminescence rather than the nanosecond-lived fluorescence of most Ag_N-DNAs.[29] It has been hypothesized

that $N_0 = 6$ Ag_N-DNAs are rod-shaped, while **Group IV** Ag_N-DNAs have a quasi-spherical geometry due to their "magic number" of 8 valence electrons.[30]

The mass spectrum of each Ag_N-DNA was analyzed in detail to determine the composition of each resolved peak, as illustrated in Fig. 1 for **I.3**. First, each peak's charge state, z, is determined from the isotope pattern, whose adjacent peaks are spaced by $1/z$. For example, **I.3** in Fig. 1 has three resolved charge states for products corresponding to nanoclusters: $z = -4$, -5, and -6 (Fig. 1a). Next, the number of stabilizing ssDNA oligomers, n_s, and the total number of silver atoms, N_{Ag}, are determined for each resolved peak. For **I.3**, mass peaks containing $n_s = 2$ and $N_{Ag} = 10$ to 18 were identified (Fig. 1a–c). Peaks at lower m/z correspond to single oligomers ($n_s = 1$) with and without a few Ag^+. The effective valence electron count, N_0, is then determined for each peak by fitting the calculated isotopic distribution to the experimental isotopic distribution (insets, Fig. 1b and c). Readers can find details about this fitting in past works.[24,27,29,30] Lastly, N_0 *vs.* N_{Ag} is plotted for all resolved products, using marker shape and color to denote the value of N_0 and marker size to denote the intensity of the mass spectral peak (Fig. 1d and e). Further details are provided in ESI section 3.†

6-electron Ag_N-DNAs with two DNA strands

We first analysed the fragmentation patterns for **Group I** Ag_N-DNAs, which are the most abundant class of Ag_N-DNAs presented in Table 1 and whose molecular formulae correspond to $n_s = 2$ and $N_0 = 6$. Fig. 2 displays N_0 *vs.* N_{Ag} values for all
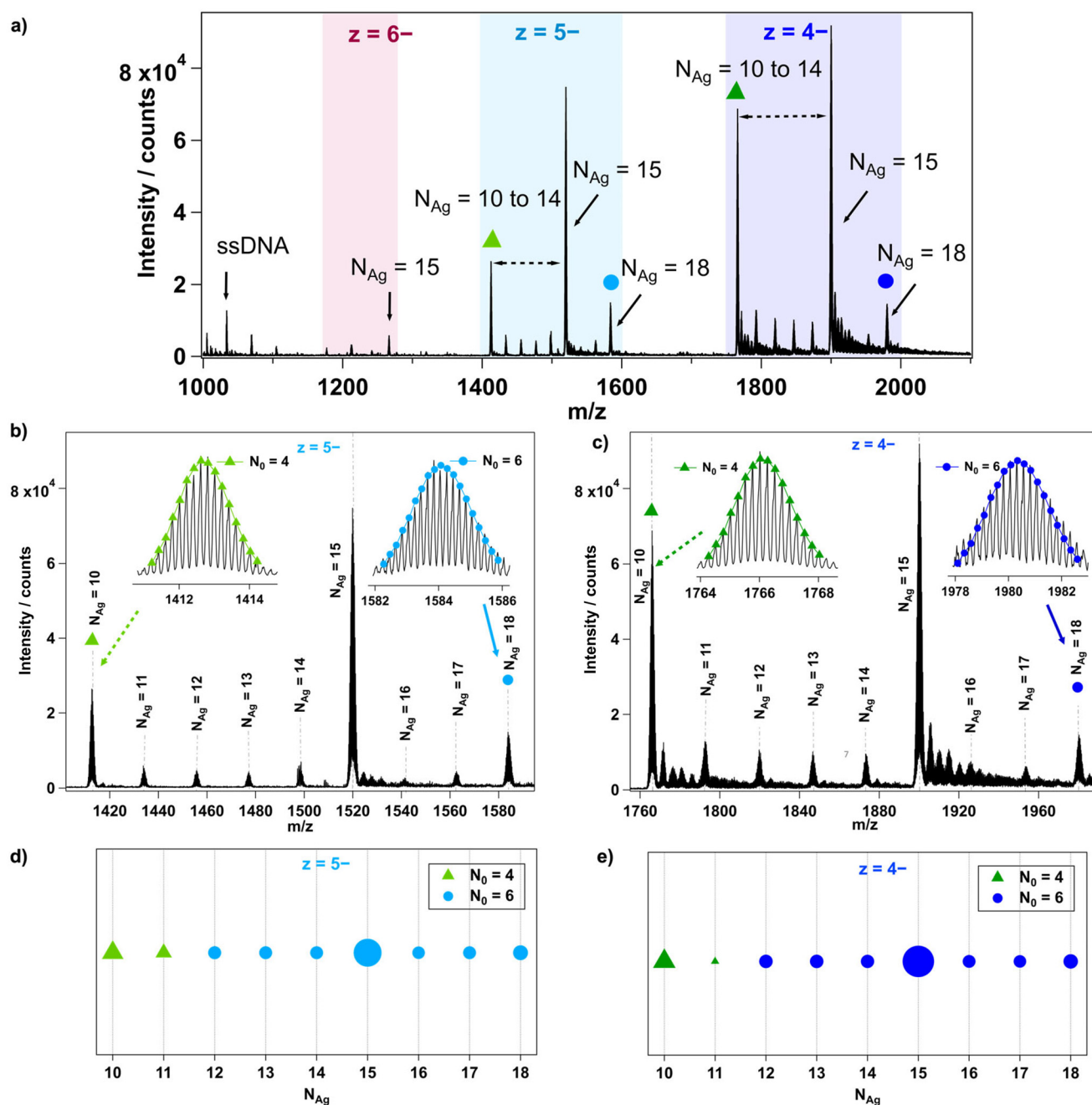
Fig. 1 (a) Mass spectra of Ag_N-DNA **I.3** highlighting the charge states (z) of the peaks and number of total silver atoms (N_{Ag}). (b) and (c) Zoomed-in mass spectra of **I.3** for charge states $z = -5$ and $z = -4$, respectively, and the inset showing the determination of N_0 values of peaks corresponding to $N_{Ag} = 18$ (blue circles) and $N_{Ag} = 10$ (green triangles). (d) and (e) Plots of N_0 values *vs.* N_{Ag} for products stabilized by two ssDNA, *i.e.*, $n_s = 2$. Marker type represents the N_0 value (green triangles and blue circles for $N_0 = 4$ and 6, respectively). Marker size represents the intensity of the mass peak in (a).

detected products at $z = -4$ and -5 charge states; products at $z = -3$ and -6 charge states are significantly less intense and are shown in Fig. S24.† A range of fragments with $n_s = 2$ and $N_0 = 6$ are resolved, suggesting that the HPLC-purified Ag_N-DNAs can lose Ag^+ during ESI-MS. Because no **Group I** Ag_N-DNA has a solved X-ray crystal structure, it is not possible to discern whether Ag^+ is removed from the Ag_N core or from sites on the

DNA template that are not incorporated into the Ag_N core, as has been resolved in Ag_N-DNA crystal structures.[34,39,40,44]

Five **Group I** Ag_N-DNAs exhibit fragments that transition from $N_0 = 6$ to $N_0 = 4$ when N_{Ag} diminishes sufficiently. The exact value of N_{Ag} at this transition ranges from 10 to 14 and, in some cases, depends somewhat on the charge state z. Fragments of **I.2**, **I.4**, and **I.6** are never observed to transition
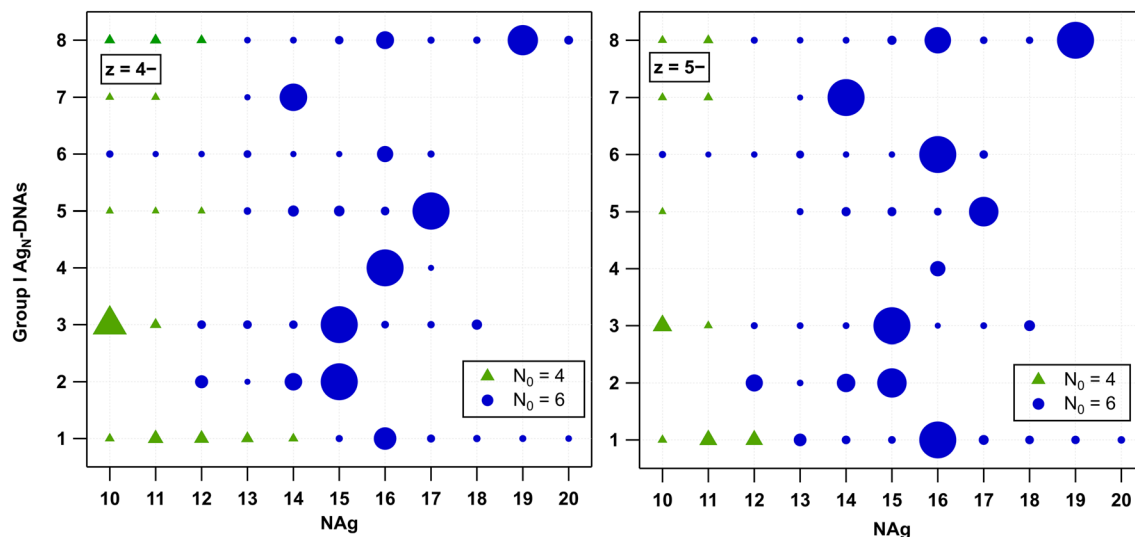
Fig. 2 Values of N_0 and N_{Ag} for **Group I** Ag_N-DNAs at $z = -4$ (left) and $z = -5$ (right). All species are stabilized by two DNA oligomers ($n_s = 2$). Products containing $N_0 = 6$ and $N_0 = 4$ are denoted by blue circles and green triangles, respectively.

to $N_0 = 4$. This diversity in the transition point from 6-electron to 4-electron clusters, as well as its dependence on the DNA template sequence and, in some cases, z, suggests that the fragmentation process of Ag_N-DNAs depends on the stability of the specific nanocluster. A similar decomposition of Ag_N-DNAs into smaller fragments under laser irradiation was investigated by Petty *et al.*, where the laser-driven degradation of an Ag_N-DNA with Ag_{10}^{6+} ($N_0 = 4$) species led to the formation of a series of fragments of Ag_6^{4+}, Ag_7^{5+}, Ag_8^{6+}, and Ag_9^{7+} species with $N_0 = 2$.[12]

No odd values of N_0 were observed for any **Group I** Ag_N-DNA. Odd N_0 values would indicate the presence of a valence electron with unpaired spin, which is expected to be energetically disfavoured. Moreover, no correlation is apparent between the previously reported circular dichroism (CD) signatures[30] and the different fragmentation patterns of these Ag_N-DNAs.

6-electron Ag_N-DNAs with three DNA strands

The fragmentation patterns of **Group II** Ag_N-DNAs are significantly more complex than those of **Group I** (Fig. S11–S13†). Past studies noted the increased fragmentation propensity of $n_s = 3$ Ag_N-DNAs under ESI-MS.[30] **II.2** has a higher hydrodynamic volume than typical $n_s = 2$ Ag_N-DNAs,[7] and the other **Group II** species are likely similar in volume. This increased size may promote fragmentation during ESI-MS.

Group II Ag_N-DNAs were observed to fragment into smaller nanoclusters by the loss of silver and/or ssDNA oligomers, forming both $n_s = 3$ and $n_s = 2$ fragments that are resolved at different charge states. To facilitate the analysis of this more complex set of processes, Fig. 3 displays mass spectral compositions separately for each Ag_N-DNA species and separates $n_s = 3$ and $n_s = 2$ products into separate panels, with the charge state indicated on the vertical axes. We first discuss **II.1**. This emitter exhibits fragments due to the loss of Ag^+ from the orig-

inal $n_s = 3$ Ag_N-DNA, as well as $n_s = 2$ fragments due to the loss of one DNA oligomer and/or silver (Fig. 3a). $n_s = 3$ fragments are most intense at the -5 charge state and retain $N_0 = 6$ at all values of N_{Ag} and z, while $n_s = 2$ fragments exhibit a wide range of N_{Ag} values at $N_0 = 6$, 4, 2, and 0. Interestingly, $N_0 = 2$ and 0 were not observed for **Group I** Ag_N-DNAs. This diversity of fragments supports that the loss of a DNA ligand produces highly reactive products that can transform into a wide range of daughter species. $N_0 = 0$ fragments may correspond to two oligomers linked by silver-mediated base pairs.[5]

II.2 and **II.3** also exhibit $n_s = 3$ and $n_s = 2$ fragments, but in contrast to **II.1**, their $n_s = 3$ fragments do transition to $N_0 = 4$ with sufficient loss of silver (Fig. 3b and c). Moreover, the loss of one ssDNA always coincides with a transition from $N_0 = 6$ to $N_0 = 4$ in **II.2** and **II.3**. This may suggest that **II.2** and **II.3** have more "tightly" bound DNA templates whose removal more significantly destabilizes the Ag_N as compared to **II.1**. Notably, **II.3** is the largest **Group II** species and loses up to 7 Ag^+ before fragments transition to $N_0 = 4$ products. The enhanced propensity of $n_s = 3$ Ag_N-DNAs to fragment during ESI-MS may also be correlated with lower stability under biological conditions, which would offset benefits of their higher quantum yields. Future studies should assess the fitness of $n_s = 3$ Ag_N-DNAs for biological imaging and sensing applications.

6-electron Ag_N-DNAs with two DNA strands and chlorido ligand(s)

We next investigate **Group III** Ag_N-DNAs, which are protected by $n_s = 2$ ssDNA and additional chlorido ligand(s). These recently discovered Ag_N-DNAs exhibit evidence for less chiral structures than Ag_N-DNAs without chloridos,[30] as well as enhanced stability in chlorine-containing buffers.[45] **III.2** through **III.6** are $(DNA)_2(Ag_{16}Cl_2)^{8+}$ types stabilised by variations of a DNA template that differ by only one nucleobase, either in position 5 or removal of the adenine in position 10
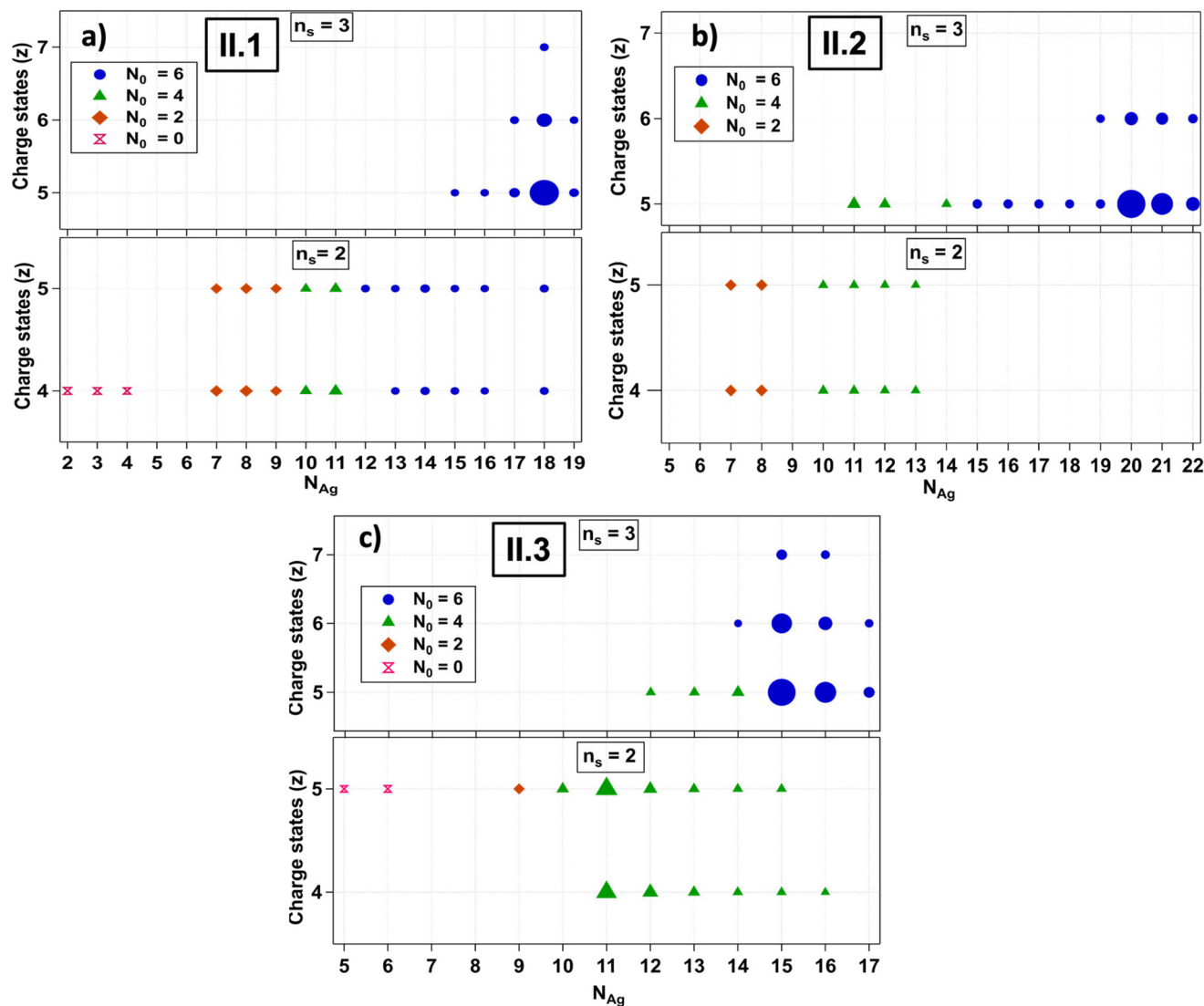
Fig. 3 Transition of N_0 with N_{Ag} for **Group II** Ag_N-DNAs: (a) **II.1**, (b) **II.2**, and (c) **II.3**. Peaks containing N_0 = 6, 4, 2, and 0 are denoted with blue circles, green triangles, ochre diamonds, and pink double triangles, respectively. Species stabilized by three and two DNA oligomers (n_s = 3 and 2) are detected.

(Table 1). These emitters have known X-ray crystal structures and very similar photophysical properties.[34,39,40,45] Fig. 4 shows all products detected for **III.2** through **III.6** at $z = -4$. $z = -5$ trends are similar and are shown in Fig. S25.† We observed that chlorido ligands are first removed as the mass of the fragmented products decreases, while preserving $N_0 = 6$. As the mass continues to decrease after chlorido and Ag^+ removal, N_0 transitions from 6 to 4 at $N_{Ag} = 11$ to 13 occur. Species containing $N_0 = 2$ are observed at $N_{Ag} = 6$ and 7, while those at $N_{Ag} = 8$ and 9 are notably absent from the mass spectra in all cases. The behaviour of **III.1** is similar to that of **III.2** and its variants as shown in Fig. S26.†

Despite having identical molecular formulae, Ag_N-DNAs in Fig. 4 exhibit differences in their fragmentation patterns. This further supports that Ag_N-DNA fragmentation under negative ion mode ESI-MS is highly sensitive to the nucleobase sequence and not solely dependent on the molecular composition of the nanocluster core. We note that while **III.4** exhibited only five resolvable products (Fig. 4), its mass spectrum also contained many ssDNA products with various contents (Fig. S16†). Thus, its lack of fragmentation products with n_s = 2 should not be construed as a sign of enhanced stability as compared to those of other Ag_N-DNAs shown in Fig. 4.

Crystal structures have confirmed that **III.2** through **III.6** are composed of a Ag_{16} core stabilized by two DNA oligomers and two chlorido ligands.[45] Thus, it is notable that a higher-mass product with $N_{Ag} = 17$ is resolved for **III.3**, **III.5**, and **III.6** (Fig. 4), as was also evident previously.[45] This additional silver is likely to be an Ag^+ bound to the DNA ligand shell but not within the Ag_N core, perhaps attached to a nucleobase that is not directly ligated to the Ag_N. Such Ag^+ is apparent in Ag_N-DNA crystal structures,[44] and it is likely that Ag^+ that is not
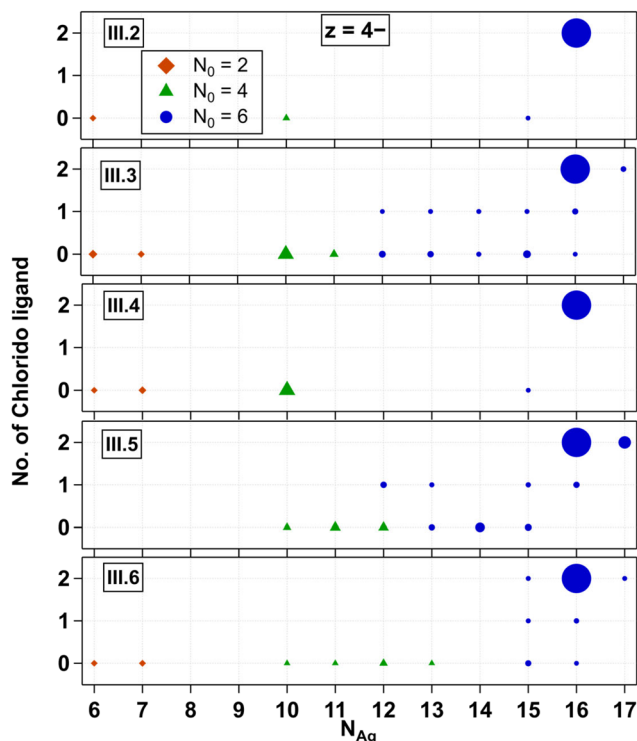
Fig. 4 N_0 and N_{Ag} of mass peaks of **Group III** Ag_N-DNAs for charge state $z = -4$. Number of chlorido ligands is represented on the vertical axis. All species are stabilized by $n_s = 2$ DNA oligomers. $N_0 = 6$, 4, and 2 are denoted by blue circles, green triangles, and ochre diamonds, respectively.

within the Ag_N core is present in other Ag_N-DNAs as well, including those reported in Fig. 2 and 3.

III.2 through **III.6** are the only HPLC-purifiable Ag_N-DNAs with currently known X-ray crystal structures that include resolved DNA ligands.[34,39,40] This provides the opportunity to use *ab initio* calculations to investigate the early stages of the fragmentation process of Ag_N-DNAs, including both structural and electronic changes during fragmentation. In particular, **III.6** has been well-studied by the Häkkinen group recently.[45–47] The fragmentation of **III.6** under ESI-MS was modelled with DFT-based molecular dynamics simulations using an implicit water solvent model. This is a compromise of the true experimental conditions under ESI-MS, which presumably desolvates the water molecules from the Ag_N-DNA. The solvent conditions involved during ESI-MS at the very beginning of the fragmentation process, including effects of droplet charging and evaporation, are unclear, and it would be computationally demanding or even intractable to model all the effects realistically. Under the simulation conditions, the Ag_{16} core was observed to dissociate into Ag_6 and Ag_{10} fragments, which separated at the point where the two chlorido ligands were attached to the Ag_{16} surface (Fig. 5a and b). The Ag_6 fragment is compact and symmetric, and octahedral in shape, while the Ag_{10} is less symmetric and prolate in shape. Despite increasing separation of the two fragments, the

HOMO–LUMO gap did not change substantially over the course of the simulation (Fig. 5a).

We next analysed the two Ag_6 and Ag_{10} fragments to determine their effective valence electron count, N_0. Fig. 5c shows the partial density of states (PDOS) for the entire system and for Ag_6 and Ag_{10} fragments. All frontier molecular orbitals of **III.6** are shown in Fig. S26,† with selected orbitals shown in Fig. 5d and e. These calculations show that the Ag_6 fragment has an occupied S state and three unoccupied P states, consistent with a $2e^-$ ($1S^2$) system, *i.e.* $N_0 = 2$. This would also be consistent with the spheroidal shape of Ag_6. The Ag_{10} fragment shows electronic states that correspond to S and P, consistent with a $4e^-$ ($1S^2 1P^2$) system. Symmetries of frontier molecular orbitals shown in Fig. 5d and e further support that the original $Ag_{16}Cl_2$ fragments into one $N_0 = 4$ Ag_{10} and one $N_0 = 2$ Ag_6. The frontier molecular orbital of the LUMO (Fig. 5d) is primarily localized on Ag_{10} and shows two nodes, while the frontier molecular orbital of the LUMO+5 is localized on Ag_6 and shows only a single node. This interpretation is consistent with our experimental observation that $(DNA)_2(Ag_{16}Cl_2)^{8+}$ fragments into $N_0 = 2$ and $N_0 = 4$ nanoclusters, with sizes in the range of Ag_6 and Ag_{10}. Thus, even at early stages in the fragmentation of Ag_N-DNAs, there is likely an electronic driving force towards fragmentation into nanoclusters with even valence electron counts, supporting our observation of only $N_0 = 0$, 2, 4, and 6 products in the mass spectra analyzed in this study.

8-electron Ag_N-DNAs (Group IV)

Finally, we examined the fragmentation patterns of Group IV Ag_N-DNAs, which have been hypothesized to be spheroidal structures rather than the rod-like structures of 6-electron Ag_N-DNAs.[29,30] Mass spectral peak intensities were the highest at $z = -5$ and -4, and these products are shown in Fig. 6. Fig. S27† shows $z = -6$ and -3 products. Just as for **Groups I, II,** and **III**, **Group IV** fragmentation products and the value of N_{Ag} at which N_0 transitions from 8 to 6 to 4 are highly dependent on the DNA template sequence. **IV.1** and **IV.2** fragment into products with $N_0 = 8$, 6, and 4. **IV.3** fragments never transition to smaller N_0; the stability of the $N_0 = 8$ products down to $N_{Ag} = 13$ contrasts with those in Fig. 2–4, in which three Ag_N-DNAs have transitioned to $N_0 = 4$ fragments at $N_{Ag} = 13$. **IV.4** fragments into products with $N_0 = 8$ and 6. **IV.1** is the only **Group 4** species with a defined absorbance peak >500 nm, which may suggest that the Ag_N core is more anisotropic than the other **Group IV** Ag_N-DNAs. Increased anisotropy could lead to a greater propensity to fragment into a variety of smaller products. X-ray crystal structures of **Group IV** Ag_N-DNAs would enable further interrogation of the fragmentation processes of these nanoclusters.

Discussion

This study investigated how Ag_N-DNAs fragment during negative ion mode ESI-MS, driven by the hypothesis that this unin-
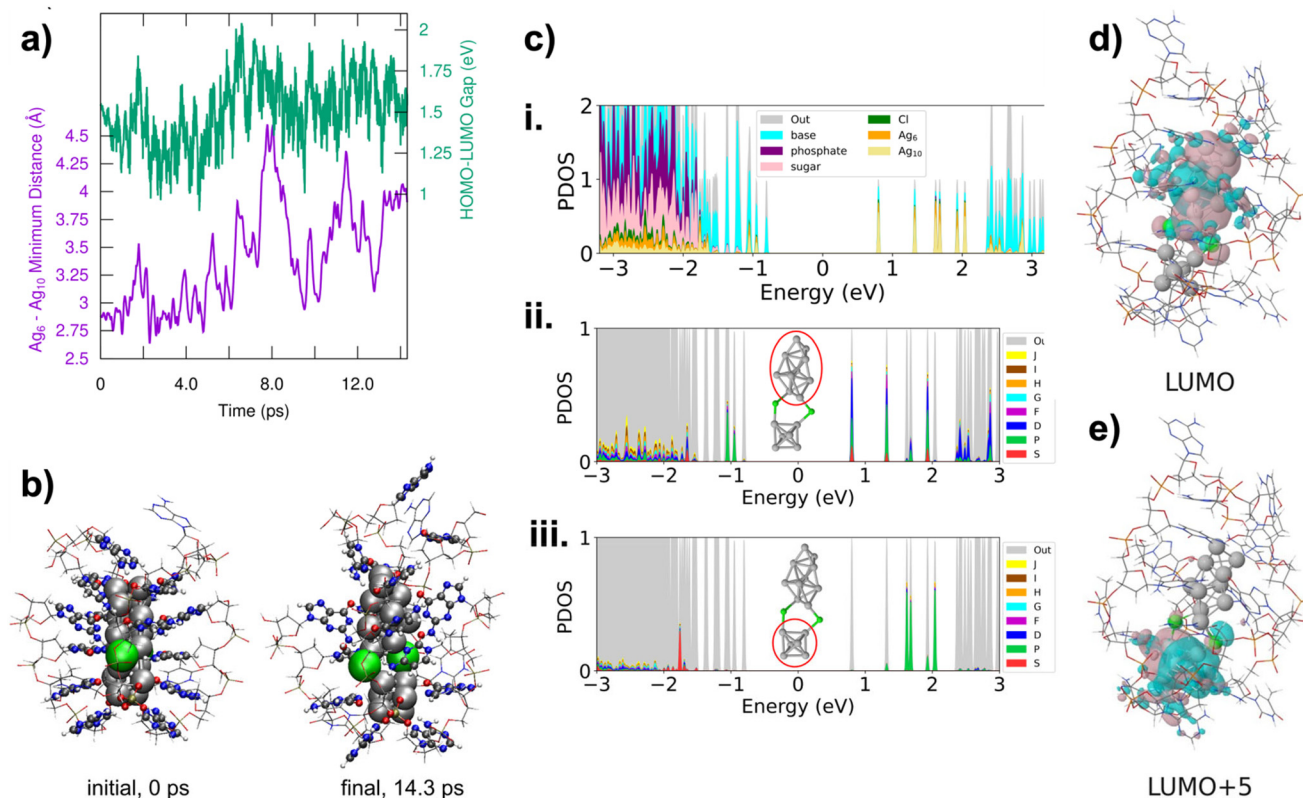
Fig. 5 Simulation of **III.6**, $(DNA)_2(Ag_{16}Cl_2)^{8+}$. (a) Time evolution of the Ag_6-Ag_{10} minimum distance (Å) and the HOMO−LUMO gap (eV). (b) Initial (0 ps) and final (14.3 ps) structures obtained from molecular dynamics simulation of **III.6**. (c) Projected density of electronic states (PDOS) to atomic orbitals of Ag_{10}, Ag_6, Cl, nucleobase, sugar, and phosphate groups for the same systems, as calculated for the final structure (14.3 ps). Coloring denotes the total weights of the specified atom groups. (ii and iii) Middle and bottom panels show analysis of the KS states of the spherical harmonics (Y_{lm}) and projected density of states (PDOS) of the Ag_{10} and Ag_6 fragments, respectively. "Out" denotes weights from spatial distribution of electrons that are not captured by the analysis. The DOS curves are obtained by broadening each discrete KS state with a 0.01 eV Gaussian. The Fermi energy is set at zero. (d) and (e) Frontier molecular orbitals of the LUMO and LUMO+5 of **III.6** calculated at the GLLB-SC functional with implicit solvent.
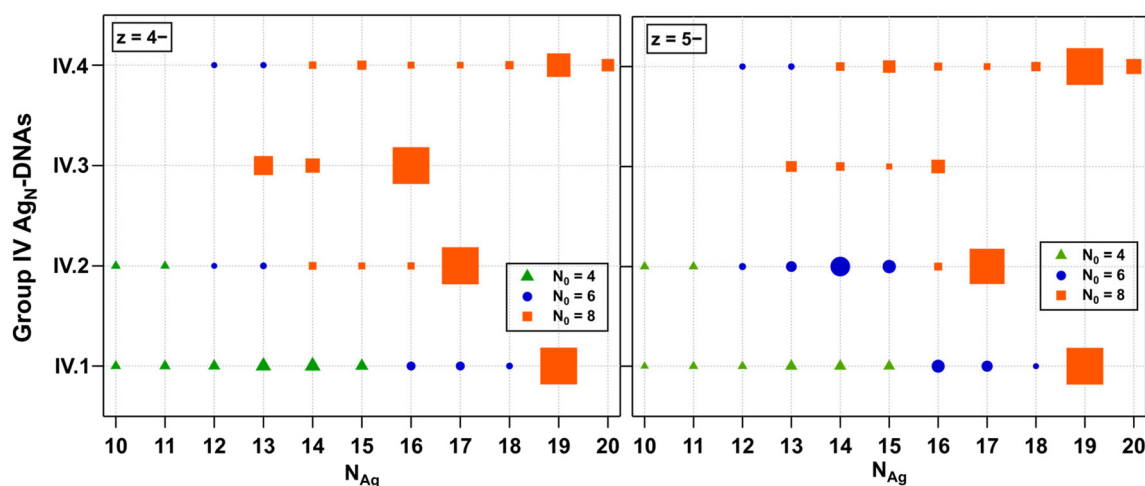

Fig. 6 N_0 and N_{Ag} values for **Group IV** Ag_N-DNAs at $z = -4$ (left) and $z = -5$ (right). Peaks corresponding to $N_0 = 8$, 6, and 4 are denoted by orange squares, blue circles, and green triangles, respectively. All products are stabilized by $n_s = 2$ DNA oligomers.

tentional fragmentation can provide insights into the chemical properties of Ag_N-DNAs without CID. Unlike monolayer-protected metal nanoclusters, which require significantly higher energies to induce fragmentation,[13] Ag_N-DNAs display multiple fragmentation products under native-like negative mode ESI-MS. This greater propensity to fragment may be due to several factors: the bulkier nature of DNA ligands compared to that of small molecule ligands, the polyelectrolyte nature of DNA and the process of partial protonation that occurs during negative ion mode ESI,[28] and the weaker Ag–N or Ag–O bonds in Ag_N-DNAs as compared to Ag–S bonds in thiol-stabilized silver nanoclusters. In ammonium acetate solution, the phosphate backbone of nucleic acids partially protonates due to proton transfer from ammonium to phosphate. This process occurs during desolvation and may occur at the same time as fragmentation events; therefore, these two processes should not be considered sequential events but rather concurrent events. Due to the harsh nature of this process, desolvation by ESI may be viewed as a "stress test" of the stability of Ag-DNAs in the gas phase.

Our analysis of 21 different Ag_N-DNAs consistently showed that the fragmentation of Ag_N-DNAs under ESI-MS strongly depends on the DNA sequence. We observed no single consistent value of total silver content N_{Ag} at which the effective valence electron count N_0 transitions to lesser values, supporting that the specific DNA template sequence strongly determines the chemical stability of Ag_N-DNAs. Even small sequence alterations that preserve the overall Ag_N-DNA structure can cause variations in stability, as is evident in **III.2** and its variants, where a single nucleobase alteration impacts fragmentation patterns.

All fragments detectable by ESI-MS in this study exhibited even valence electron counts: $N_0 = 0, 2, 4, 6,$ or 8. The spectral purity of the 21 HPLC-purified Ag_N-DNAs strongly supports that the smaller nanocluster products detected in mass spectra were not present in any appreciable quantity before ESI-MS and therefore formed due to fragmentation. Because such fragments may include species that are transiently stable in the gas phase but not stable in solution, the absence of odd valence electron counts is significant. Simulation of **III.6** further supports the strong electronic driving force towards forming fragments that retain even values of N_0, as electronic states begin to localize on fragments even in early stages. Thus, it is highly unlikely that Ag_N-DNAs with odd valence electron counts would be stable in solution. We suggest that reports of solution-stable Ag_N-DNAs with odd values of N_0 may be affected by slight miscalibration of the mass spectrometer, as precision to a single proton is required for accurate N_0 assignment, and this level of precision can be challenging to achieve at high m/z values where Ag_N-DNAs are detected by ESI-MS.

Our findings also support the presence of Ag^+ ions that are coordinated to the DNA ligands yet not within the Ag_N core in HPLC-purified Ag_N-DNAs. We observed multiple examples of these products for $(DNA)_2(Ag_{16}Cl_2)^{8+}$ with a known X-ray crystal structure (Fig. 4), and possible products for other Ag_N-DNAs are evident (Fig. 2, 3 and 5). If easily removed by ESI-MS, such Ag^+ may be weakly bound and could have implications for the cytotoxicity of those Ag_N-DNA species. Future efforts are needed to resolve Ag_N-DNA crystal structures and thereby assign nanocluster composition in conjunction with ESI-MS, as well as to investigate whether loosely bound Ag^+ influences factors such as the cytotoxicity of Ag_N-DNAs, which will be essential for developing their biomedical applications. Moreover, our findings strongly suggest that cytotoxicity will depend on the DNA template sequence of a specific Ag_N-DNA, as has been previously reported.[48]

The information this study provides on the degree of lability of DNA and chlorido ligands for specific Ag_N-DNA species could inform novel strategies to tune solution-phase Ag_N-DNA chemical transformations and ligand protection. Ag^+ shedding in solution may drive the transformation of Ag_N-DNAs into smaller Ag_N-DNAs, including those with lower N_0 values that will display significantly shifted emission wavelengths.[49] We propose that such a transformation, accompanied by the loss of Ag^+, or movement of Ag^+ away from or towards the Ag_N core, is the underlying mechanism of colorimetric Ag_N-DNA sensing schemes such as NanoCluster Beacons,[4,50–52] which generally exhibit red-green transitions. Thus, an inherent degree of lability may be key to Ag_N-DNA sensing schemes. Moreover, the propensity to fragment under ESI-MS may correlate with emitter stability and degradation of Ag_N-DNAs *in vivo*. Ag_N-DNAs with chlorido ligands demonstrate exceptional stability in physiological buffers, and the presence of chloride ions in solution can dramatically enhance Ag_N-DNA emission intensity.[2] Thus, investigating the lability of chlorido ligands in the gas phase could reveal mechanisms to more controllably protect Ag_N-DNAs with chlorides and improve their biocompatibility. Finally, similar methods may be useful for investigating the properties of noble metal nanoclusters stabilized by other biomolecular ligands.[53–55]

Conclusion

Detailed analysis of the fragmentation patterns of 21 HPLC-purified Ag_N-DNAs under negative ion mode ESI-MS shows that fragmentation is strongly dependent on the Ag_N-DNA template sequence. Ag_N-DNAs appear to lose silver including Ag^+ during ESI-MS, and the fragmentation patterns of Ag_{16}-DNAs of known X-ray crystal structures confirm that a fraction of these Ag^+ may be bound to the DNA ligand shell but not a part of the initial Ag_N core. With sufficient loss of silver, the nanocluster's effective valence electron count, N_0, can decrease. The detected nanocluster fragments only exhibit even values of N_0, strongly supporting the likelihood that Ag_N-DNAs with odd valence electron counts are unlikely to be stable in solution. Molecular dynamics simulations, with forces calculated from density functional theory, of an Ag_{16}-DNA with a known crystal structure support the dissociation of the nanocluster core into two smaller nanocluster species, each containing an even number of valence electrons, which is further supported by

the symmetry of the frontier molecular orbitals of the fragment species. Together, these results provide new insights into the chemistry of Ag_N-DNAs in the gas phase and may have relevance to both chemical transformations of Ag_N-DNAs that enable colorometric sensing schemes and degradation of Ag_N-DNAs *in vivo*, where loss of Ag^+ may contribute to cytotoxicity. Future mass spectral studies using tools such as CID and TIMS may shed further light on chemical reactions involving Ag_N-DNAs.

Methods

Synthesis and purification of Ag_N-DNAs

Ag_N-DNAs were synthesized by the addition of stoichiometric amounts of $AgNO_3$ to an aqueous solution of DNA oligomer (Integrated DNA Technologies, standard desalting) in 10 mM ammonium acetate (pH 7), followed by the partial reduction of silver content using a 0.5 molar ratio of a freshly prepared aqueous solution of $NaBH_4$. The solution was kept at 4 °C (or stated otherwise) in the dark until concentration by spin filtering and then purification using reverse-phase HPLC. Following HPLC, the solvent was exchanged into 10 mM ammonium acetate, pH 7. Details on the synthesis and purification methods, HPLC chromatograms and mass spectra of the Ag_N-DNAs have been previously reported.[2,29,30]

Mass spectrometry

Electrospray ionization mass spectrometry (ESI-MS) was performed using a Waters Xevo G2-XS QTof. Samples were directly injected at 0.1 mL min^{-1} in negative ion mode with a 2 kV capillary voltage, 30 V cone voltage and no collision energy. Spectra were collected from 1000 to 4000 *m/z* with an integration time of 1 s. Source and desolvation temperatures were 80 and 150 °C, respectively. Gas flows were 45 L h^{-1} for the cone and 450 L h^{-1} for the desolvation. Samples were injected with 50 mM NH_4OAc – MeOH (80 : 20) solution at pH 7. The mass spectra of Ag_N-DNAs are shown in Fig. S3 to S21.† Determination of nanocluster size (total number of silver N, ligand composition *i.e.*, the number of DNA strands n_s, and the presence of additional chlorido ligands) and the overall charge, Q_c (and hence determining the number of effective valence electron count N_0) was performed by fitting the calculated isotopic distribution of the Ag_N-DNA to the experimental spectra (details in the ESI†). Calculated isotopic distributions were obtained from MassLynx using the chemical formula and corrected for the overall positive charge (oxidation state, Q_c) of the nanocluster core.

Molecular dynamics and density functional theory calculations

DFT was implemented in the software GPAW,[56,57] with real space grids with a grid spacing of 0.2 and Perdew–Burke–Ernzerhof (PBE) functional.[58] The nanocluster structure was created based on the experimentally solved crystal structure by Vosch, *et al.*[34] which was later confirmed to include 2 Cl ligands on the Ag core surface and computationally analyzed as a corrected model structure.[45,47] An implicit water solvent model was used in all calculations.[47,59] PBE-optimized coordinates of the nanocluster were used as a starting structure for the molecular dynamics simulation. Molecular dynamics (MD) was performed using a Langevin thermostat with a 2 fs time step and a 0.01 fs friction parameter. Masses of hydrogen atoms were treated as those of deuterium atoms. The total length of the MD run was 14.3 ps, from which heating to the target temperature of 300 K took ∼3 ps was performed. To reveal the possible fragmentation mechanism, the minimum distance between Ag_6 and Ag_{10} parts of the metal core was analyzed from the MD trajectory. The last snapshot structure at 14.3 ps was then used for electronic structure analysis using the GLLB-SC xc-functional.[60] Full details regarding DFT and MD calculations are provided in the ESI.†

Data availability

The data supporting this article have been included as part of the ESI† in the form of mass spectral data graphs and tables.

Conflicts of interest

There are no conflicts to declare.

Acknowledgements

References

1 A. Gonzàlez-Rosell, C. Cerretani, P. Mastracco, T. Vosch and S. M. Copp, *Nanoscale Adv.*, 2021, **3**, 1230–1260.

2 R. Guha, M. Rafik, A. Gonzàlez-Rosell and S. M. Copp, *Chem. Commun.*, 2023, **59**, 10488–10491.

3 Y.-A. Chen, J. M. Obliosca, Y.-L. Liu, C. Liu, M. L. Gwozdz and H.-C. Yeh, *J. Am. Chem. Soc.*, 2015, **137**, 10476–10479.

4 X. Yan, J. Sun, X. E. Zhao, R. Wang, X. Wang, Y. N. Zuo, W. Liu, R. Kong and S. Zhu, *Microchim. Acta*, 2018, **185**, 403.

5 R. Guha and S. M. Copp, in *Modern Avenues in Metal-Nucleic Acid Chemistry*, ed. J. Müller and B. Lippert, CRC Press, 2023, ch. 12, pp. 291–342.

6 S. A. Bogh, M. R. Carro-Temboury, C. Cerretani, S. M. Swasey, S. M. Copp, E. G. Gwinn and T. Vosch, *Methods Appl. Fluoresc.*, 2018, **6**, 024004.

7 V. A. Neacșu, C. Cerretani, M. B. Liisberg, S. M. Swasey, E. G. Gwinn, S. M. Copp and T. Vosch, *Chem. Commun.*, 2020, **56**, 6384–6387.

8 V. Rück, N. K. Mishra, K. K. Sørensen, M. B. Liisberg, A. B. Sloth, C. Cerretani, C. B. Mollerup, A. Kjaer, C. Lou, K. J. Jensen and T. Vosch, *J. Am. Chem. Soc.*, 2023, **145**, 16771–16777.

9 X. Wang, M. B. Liisberg, G. L. Nolt, X. Fu, C. Cerretani, L. Li, L. A. Johnson, T. Vosch and C. I. Richards, *ACS Nano*, 2023, **17**, 12862–12874.

10 J. Sharma, H. C. Yeh, H. Yoo, J. H. Werner and J. S. Martinez, *Chem. Commun.*, 2011, **47**, 2294–2296.

11 J. M. Obliosca, C. Liu, R. A. Batson, M. C. Babin, J. H. Werner and H.-C. Yeh, *Biosensors*, 2013, **3**, 185–200.

12 C. J. Setzler, C. A. Arrington, D. Lewis and J. T. Petty, *J. Phys. Chem. B*, 2023, **127**, 10851–10860.

13 P. Chakraborty, S. Malola, M. Neumaier, P. Weis, H. Häkkinen and M. M. Kappes, *Angew. Chem., Int. Ed.*, 2023, **62**, e202305836.

14 L. Zhang, M. Guo, J. Zhou, C. Fang and X. Sun, *Small*, 2023, **19**, e2301633.

15 T. Chen, Q. Yao, R. R. Nasaruddin and J. Xie, *Angew. Chem., Int. Ed.*, 2019, **58**, 11967–11977.

16 H. Gholipour-Ranjbar, Deepika, P. Jena and J. Laskin, *Commun. Chem.*, 2022, **5**, 130.

17 Z. Wu, D.-e. Jiang, E. Lanni, M. E. Bier and R. Jin, *J. Phys. Chem. Lett.*, 2010, **1**, 1423–1427.

18 A. Baksi, E. K. Schneider, P. Weis, K. R. Krishnadas, D. Ghosh, H. Hahn, T. Pradeep and M. M. Kappes, *J. Phys. Chem. C*, 2019, **123**, 28477–28485.

19 M. Neumaier, A. Baksi, P. Weis, E. K. Schneider, P. Chakraborty, H. Hahn, T. Pradeep and M. M. Kappes, *J. Am. Chem. Soc.*, 2021, **143**, 6969–6980.

20 S. Biswas, S. Das and Y. Negishi, *Coord. Chem. Rev.*, 2023, **492**, 215255.

21 R. Jin, *Nanoscale*, 2010, **2**, 343–362.

22 R. H. Adnan, J. M. L. Madridejos, A. S. Alotabi, G. F. Metha and G. G. Andersson, *Adv. Sci.*, 2022, **9**, 2105692.

23 E. L. Albright, T. I. Levchenko, V. K. Kulkarni, A. I. Sullivan, J. F. DeJesus, S. Malola, S. Takano, M. Nambo, K. Stamplecoskie, H. Häkkinen, T. Tsukuda and C. M. Crudden, *J. Am. Chem. Soc.*, 2024, **146**, 5759–5780.

24 D. Schultz and E. G. Gwinn, *Chem. Commun.*, 2012, **48**, 5748–5750.

25 K. Koszinowski and K. Ballweg, *Chem. – Eur. J.*, 2010, **16**, 3285–3290.

26 D. Schultz, K. Gardner, S. S. R. Oemrawsingh, N. Markešević, K. Olsson, M. Debord, D. Bouwmeester and E. Gwinn, *Adv. Mater.*, 2013, **25**, 2797–2803.

27 S. M. Copp, D. Schultz, S. Swasey, J. Pavlovich, M. Debord, A. Chiu, K. Olsson and E. Gwinn, *J. Phys. Chem. Lett.*, 2014, **5**, 959–963.

28 E. Largy, A. König, A. Ghosh, D. Ghosh, S. Benabou, F. Rosu and V. Gabelica, *Chem. Rev.*, 2021, **122**, 7720–7839.

29 A. González-Rosell, R. Guha, C. Cerretani, V. Rück, M. B. Liisberg, B. B. Katz, T. Vosch and S. M. Copp, *J. Phys. Chem. Lett.*, 2022, **13**, 8305–8311.

30 R. Guha, A. Gonzàlez-Rosell, M. Rafik, N. Arevalos, B. B. Katz and S. M. Copp, *Chem. Sci.*, 2023, **14**, 11340–11350.

31 J. T. Petty, O. O. Sergev, A. G. Kantor, I. J. Rankine, M. Ganguly, F. D. David, S. K. Wheeler and J. F. Wheeler, *Anal. Chem.*, 2015, **87**, 5302–5309.

32 J. T. Petty, O. O. Sergev, M. Ganguly, I. J. Rankine, D. M. Chevrier and P. Zhang, *J. Am. Chem. Soc.*, 2016, **138**, 3469–3477.

33 K. G. Stamplecoskie and P. Aminfar, *Chem. Mater.*, 2024, **36**(19), 9003–9012.

34 C. Cerretani, J. Kondo and T. Vosch, *RSC Adv.*, 2020, **10**, 23854–23860.

35 P. Mastracco, A. Gonzàlez-Rosell, J. Evans, P. Bogdanov and S. M. Copp, *ACS Nano*, 2022, **16**, 16322–16331.

36 S. M. Copp, P. Bogdanov, M. Debord, A. Singh and E. Gwinn, *Adv. Mater.*, 2016, **28**, 3043.

37 S. M. Swasey, S. M. Copp, H. C. Nicholson, A. Gorovits, P. Bogdanov and E. G. Gwinn, *Nanoscale*, 2018, **10**, 19701–19705.

38 S. M. Copp, S. M. Swasey, A. Gorovits, P. Bogdanov and E. G. Gwinn, *Chem. Mater.*, 2020, **32**, 430–437.

39 C. Cerretani, H. Kanazawa, T. Vosch and J. Kondo, *Angew. Chem., Int. Ed.*, 2019, **58**, 17153–17157.

40 C. Cerretani, J. Kondo and T. Vosch, *CrystEngComm*, 2020, **22**, 8136–8141.

41 A. Gonzàlez-Rosell and S. M. Copp, *Acc. Chem. Res.*, 2024, **57**, 2117–2129.

42 E. Bethur, R. Guha, Z. Zhao, B. B. Katz, P. D. Ashby, H. Zeng and S. M. Copp, *ACS Nano*, 2024, **18**, 3002–3010.

43 M. S. Blevins, D. Kim, C. M. Crittenden, S. Hong, H.-C. Yeh, J. T. Petty and J. S. Brodbelt, *ACS Nano*, 2019, **13**, 14070–14079.

44 D. J. E. Huard, A. Demissie, D. Kim, D. Lewis, R. M. Dickson, J. T. Petty and R. L. Lieberman, *J. Am. Chem. Soc.*, 2019, **141**, 11465–11470.

45 A. Gonzàlez-Rosell, S. Malola, R. Guha, N. R. Arevalos, M. F. Matus, M. E. Goulet, E. Haapaniemi, B. B. Katz, T. Vosch, J. Kondo, H. Häkkinen and S. M. Copp, *J. Am. Chem. Soc.*, 2023, **145**, 10721–10729.

46 S. Malola and H. Häkkinen, *Chem. Commun.*, 2024, **60**, 3315–3318.

47 S. Malola, M. F. Matus and H. Häkkinen, *J. Phys. Chem. C*, 2023, **127**, 16553–16559.

48 N. Bossert, D. de Bruin, M. Götz, D. Bouwmeester and D. Heinrich, *Sci. Rep.*, 2016, **6**, 37897.

49 S. M. Copp and A. Gonzàlez-Rosell, *Nanoscale*, 2021, **13**, 4602–4613.

50 J. M. Obliosca, M. C. Babin, C. Liu, Y. L. Liu, Y. A. Chen, R. A. Batson, M. Ganguly, J. T. Petty and H. C. Yeh, *ACS Nano*, 2014, **8**, 10150–10160.

51 Y.-A. Kuo, O. S. Zhao, S. Hong, T. D. Nguyen, Y.-I. Chen, H.-C. Li and T. Yeh, *Biophys. J.*, 2021, **120**, 272a.

52 Y.-A. Chen, H. T. Vu, Y.-L. Liu, Y.-I. Chen, T. D. Nguyen, Y.-A. Kuo, S. Hong, Y.-A. Chen, S. Carnahan, J. T. Petty and H.-C. Yeh, *Chem. Commun.*, 2019, **55**, 462–465.

53 E. Lopez-Martinez, D. Gianolio, S. Garcia-Orrit, V. Vega-Mayoral, J. Cabanillas-Gonzalez, C. Sanchez-Cano and A. L. Cortajarena, *Adv. Opt. Mater.*, 2022, **10**, 2101332.

54 S. Gregersen, T. Vosch and K. J. Jensen, *Chem. – Eur. J.*, 2016, **22**, 18492–18500.

55 S. C. Scott, J. A. Cadge, G. K. Boden, J. F. Bower and C. A. Russell, *Angew. Chem., Int. Ed.*, 2023, **62**, e202301526.

56 J. J. Mortensen, A. H. Larsen, M. Kuisma, A. V. Ivanov, A. Taghizadeh, A. Peterson, A. Haldar, A. O. Dohn, C. Schäfer, E. Jónsson, E. D. Hermes, F. A. Nilsson, G. Kastlunger, G. Levi, H. Jónsson, H. Häkkinen, J. Fojt, J. Kangsabanik, J. Sødequist, J. Lehtomäki, J. Heske, J. Enkovaara, K. T. Winther, M. Dulak, M. M. Melander, M. Ovesen, M. Louhivuori, M. Walter, M. Gjerding, O. Lopez-Acevedo, P. Erhart, R. Warmbier, R. Würdemann, S. Kaappa, S. Latini, T. M. Boland, T. Bligaard, T. Skovhus, T. Susi, T. Maxson, T. Rossi, X. Chen, Y. L. A. Schmerwitz, J. Schiøtz, T. Olsen, K. W. Jacobsen and K. S. Thygesen, *J. Chem. Phys.*, 2024, **160**(9), 092503.

57 J. Enkovaara, C. Rostgaard, J. J. Mortensen, J. Chen, M. Dułak, L. Ferrighi, J. Gavnholt, C. Glinsvad, V. Haikola, H. A. Hansen, H. H. Kristoffersen, M. Kuisma, A. H. Larsen, L. Lehtovaara, M. Ljungberg, O. Lopez-Acevedo, P. G. Moses, J. Ojanen, T. Olsen, V. Petzold, N. A. Romero, J. Stausholm-Møller, M. Strange, G. A. Tritsaris, M. Vanin, M. Walter, B. Hammer, H. Häkkinen, G. K. Madsen, R. M. Nieminen, J. K. Nørskov, M. Puska, T. T. Rantala, J. Schiøtz, K. S. Thygesen and K. W. Jacobsen, *J. Phys.: Condens. Matter*, 2010, **22**, 253202.

58 J. P. Perdew, K. Burke and M. Ernzerhof, *Phys. Rev. Lett.*, 1996, **77**, 3865–3868.

59 A. Held and M. Walter, *J. Chem. Phys.*, 2014, **141**, 174108.

60 M. Kuisma, J. Ojanen, J. Enkovaara and T. T. Rantala, *Phys. Rev. B: Condens. Matter Mater. Phys.*, 2010, **82**, 115106.